Mechanics Promotes Coherence in Heterogeneous Active Media

Soling Zimik[1,*] and Sitabhra Sinha[1,2]
[1]The Institute of Mathematical Sciences, CIT Campus, Taramani, Chennai 600113, India
[2]Homi Bhabha National Institute, Anushaktinagar, Mumbai 400094, India

(Received 10 September 2024; accepted 30 October 2025; published 11 December 2025)

Synchronization of activity among myocytes constituting vital organs, e.g., the heart, is crucial for physiological functions. Self-organized coordination in such heterogeneous ensemble of excitable and oscillatory cells is therefore of clinical importance. We show by varying the strength of intercellular coupling and the electrophysiological diversity, a wide range of collective behavior emerges including clusters of synchronized activity. Strikingly, stretch-activated currents allow waves of mechanical deformation to alter the activity of neighboring cells, promoting robust global coherence.

DOI: 10.1103/8gqg-rsrl

Cells whose contractility are mediated by electrical signals are central to many vital physiological processes [1–3]. Examples include the myocytes in the heart and smooth muscle cells in the uterus and the gastrointestinal (GI) tract [4–6]. While the changes in the electrical state of the cells that lead to contractions of the myofibrils (viz., excitation-contraction coupling) is well studied, the emergent behavior resulting from interactions between cells via electrical as well as mechanical means is less understood. The problem is further compounded by most biological tissues being heterogeneous mixtures of distinct cell types with characteristic activity patterns, making the system-wide coherence even more remarkable. As intercellular interactions are believed to underlie the observed tissue-scale synchronization of activity that is functionally crucial, e.g., in the pumping action of the heart, it is important to understand how global coordination is achieved by local electromechanical interactions.

Cells stimulated by electrical signals typically exhibit *excitability* [7–10], characterized by a nonlinear response of the transmembrane potential. In excitable (E) cells, this manifests as an action potential elicited by a supra-threshold stimulus, while oscillatory (O) cells spontaneously generate periodic pulses of activity. These distinct cell types coexist in many natural settings, such as, the GI tract [11], the sino-atrial node (the natural pacemaker of the heart [12,13]) or diseased cardiac tissue [14,15]. Note that O cells may also represent cellular aggregates comprising excitable and passive cells (e.g., fibroblasts) coupled by gap junctions that give rise to emergent oscillations [16,17]. These are of relevance in the uterus, whose isolated cells cannot exhibit autonomous activity but at late stages of pregnancy, increased gap junction expression is accompanied by local spontaneous oscillations that evolve into organ-wide contractions leading to childbirth [5]. As the relative density of such cells and the strength of their coupling can change over time, e.g., in the embryonic heart [18,19], the gravid uterus [5,20,21], or as a result of disease-induced physiological alterations [14,22], it is essential to explicate the collective dynamics resulting from electrical and mechanical interactions between these heterogeneous cell types. In particular, we want to understand the mechanisms promoting robust coherence of organ-wide periodic activity, whose breakdown leads to pathological outcomes such as cardiac arrhythmia, irritable bowel syndrome, or premature contractions leading to preterm birth. A crucial piece of the puzzle revealed relatively recently follows from the mechanical contraction of a cell triggered by its electrical excitation [9,23]. This stress affects the activation of neighboring cells via mechanosensitive pathways, e.g., by inducing stretch-activated current (I_{sac}) [Figs. 1(a) and 1(b)]. Thus, a propagating excitation wave will be preceded by a mechanical deformation (stretching) of cells anterior to the wavefront, thereby stimulating I_{sac} (and hence excitation) in these cells [Figs. 1(c)–1(e)].

In this Letter we show how such electromechanical interactions between cells can significantly enhance synchronized activity in the system. Even when the electrotonic coupling via gap junctions is weak, cells can coordinate by the tension-induced electrical activity, resulting in the emergence of robust coherence, with almost all cells oscillating in phase. The key role played by mechanics in promoting synchrony is demonstrated in electrically heterogeneous media comprising E and O cells [17,24–26]. As the relative density of the distinct cell types, and/or the strengths of electrotonic coupling between cells are varied, their collective activity exhibits transitions between a variety of spatiotemporal patterns, e.g., spatially localized clusters of excitation eventually merging to states characterized by

*Present address: Indian Institute of Science Education and Research (IISER) Thiruvananthapuram, Vithura, Maruthamala P.O., Trivandrum 695551, India.

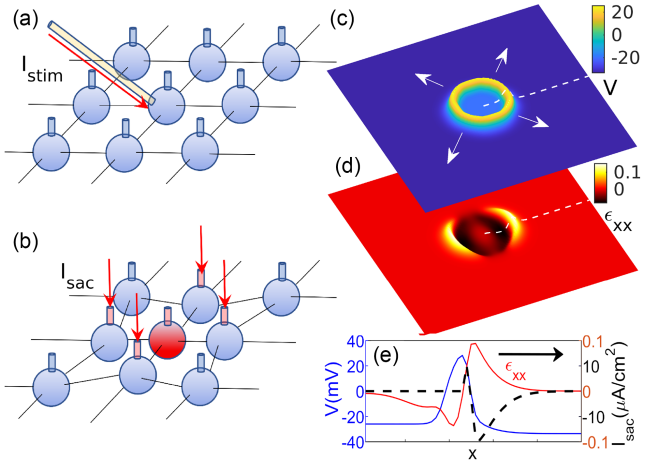

FIG. 1. Intercellular electromechanical coupling promotes propagation of activity across excitable media. (a),(b) Excitable tissue schematically represented as a regular lattice of cells, each coupled to its neighbors both electrically and mechanically. (a) Activation of the central cell upon stimulation by current $I_{\rm stim}$ results in a contraction that (b) locally deforms the neighborhood and induces activity in surrounding cells by allowing current $I_{\rm sac}$ through their stretch-activated channels. (c),(d) Point stimulation at the center of a domain results in propagation (indicated by arrows) of an excitation front in the membrane potential V (c), accompanied by a deformation manifesting as a wave in the normal strain field, whose x component, ϵ_{xx}, is shown in (d). The spatial profiles of the various fields (blue: V, red: ϵ_{xx}, black: $I_{\rm sac}$) along the broken line in (c),(d) are indicated in (e). Note the deformation at locations anterior to the excitation front, moving in the direction of the arrow, results from stretching (+ve strain) induced in its neighbors by an excited cell contracting (−ve strain). This generates a current $I_{\rm sac}$ ($< 0 \Rightarrow$ current flows into a cell) resulting in activation (see V).

traveling waves, ultimately leading to coherence. These patterns can be associated with various abnormal physiological rhythms [27,28], making our results potentially of clinical relevance.

The time evolution of the electrical state (transmembrane potential field V) of a tissue considered as a continuum is given by

$$\partial V/\partial t = (I/C_m) + \nabla.(D\nabla V) - \nabla.(V\dot{\mathbf{U}}), \qquad (1)$$

where the last (convective) term represents the change in potential resulting from tissue deformation, which is absent in models that do not consider the current ($I_{\rm sac}$) arising from mechanical stretching. The membrane capacitance $C_m = 20\ \mu{\rm F\,cm^{-2}}$, D is the diffusion coefficient representing the gap-junctional conductances that can vary across space, and the current $I = -I_{\rm ion} - I_{\rm sac}$. For most of the results discussed here, the ionic current $I_{\rm ion}$ for each cell is described according to the Morris-Lecar model [29]: $I_{\rm ion} = g_K n(V-E_K) + g_{Ca} m_\infty (V-E_{Ca}) + g_L(V-E_L) + I_{\rm bas}$, the first three terms representing a K^+ current determining the recovery, a Ca^{2+} current providing the initial excitation and a membrane leakage current, respectively. The spatially varying basal current $I_{\rm bas}$ determines whether an isolated cell is excitable, or spontaneously oscillating with different frequencies (that depend on the magnitude of $I_{\rm bas}$ [30]) following a Hopf bifurcation for $I_{\rm bas} > 90$ [39]. Here, n is a gating variable for the K^+ current, which evolves as $dn/dt = (n_\infty - n)/\tau_n$, with asymptotic value $n_\infty = [1 + \tanh(V - V_3)/V_4]/2$ and characteristic time $\tau_n = 25/\cosh([V - V_3]/2V_4)$, the parameters being set to $V_3 = 2$, $V_4 = 30$ [40]. The kinetics of the Ca^{2+} channel is assumed to be relatively faster and thus, the asymptotic value $m_\infty = [1 + \tanh(V - V_1)/V_2]/2$ is used. The parameters are chosen to be $g_L = 2$, $g_{Ca} = 4.4$, $g_K = 8$ ($m\mho\,{\rm cm^{-2}}$), $V_1 = -1.2$, $V_2 = 18$, $E_K = -84$, $E_{Ca} = 120$, and $E_L = -60$ (mV). Note that we have also used the more detailed McAllister-Noble-Tsien (MNT) model for myocardial Purkinje fibers [31] for additional simulations [30].

The stretch-activated current $I_{\rm sac} = g_{\rm sac} E(V - V_{\rm sac})$ results from mechanical interactions between the cells, with $g_{\rm sac}$ and $V_{\rm sac}$ representing conductance and reversal potential, respectively, of the ion channel [32,41,42]. As stretching the cell results in the opening of the channel [43,44], $I_{\rm sac}$ is finite if the normal components of the strain ϵ are positive, measured as $E = \sqrt{\epsilon_{xx}^2 \Theta(\epsilon_{xx}) + \epsilon_{yy}^2 \Theta(\epsilon_{yy})}$, where $\epsilon_{ij} = \frac{1}{2}(\partial U_i/\partial r_j + \partial U_j/\partial r_i)$ with $\{i,j\} = \{x,y\}$, U_i are the components of the displacement vector field $\mathbf{U}$, $\mathbf{r}$ is the position vector, and $\Theta(\,)$ is the Heaviside step function. We assume the medium to be a linear isotropic elastic solid in an overdamped environment [45,46], such that the displacement field evolves as

$$\partial \mathbf{U}/\partial t = \nabla.(\boldsymbol{\sigma}^{\rm passive} + \boldsymbol{\sigma}^{\rm active}), \qquad (2)$$

where the passive component of the stress is determined by the material properties of the solid, viz., $\sigma_{ij}^{\rm passive} = \lambda \delta_{ij}\epsilon_{kk} + 2\mu\epsilon_{ij}$, where δ_{ij} is the Kronecker delta function and λ, μ are the Lamé parameters [47]. The active component $\sigma_{ij}^{\rm active} = T^{\rm active}\delta_{ij}$ results from the active tension $T^{\rm active}$ induced by intrinsic electrical excitation of a cell and evolves with the normalized transmembrane potential $\mathcal{V}$ [$= (V - V_{\rm min})/(V_{\rm max} - V_{\rm min})$, where $V_{\rm max} = 30$ mV and $V_{\rm min} = -50$ mV are the highest and lowest V values attained during an action potential] as,

$$\frac{dT^{\rm active}}{dt} = K(\alpha\mathcal{V} - T^{\rm active}), \qquad (3)$$

where $K(\mathcal{V})$ is a function that controls the timescale of active stress, viz., $K(\mathcal{V}) = 0.02(0.2)$ for $\mathcal{V} < -0.01$ ($\mathcal{V} > -0.01$) and $\alpha(= 0.3)$ controls the magnitude of the contraction impulse [48]. Thus, Eqs. (1)–(3) describe the electromechanical coupling in the medium. Cell activation (rise in V) increases the tension $T^{\rm active}$ inside the cell [Eq. (3)], causing its contraction, which in turn stretches its neighboring cells and activates $I_{\rm sac}$ in the neighboring cells.

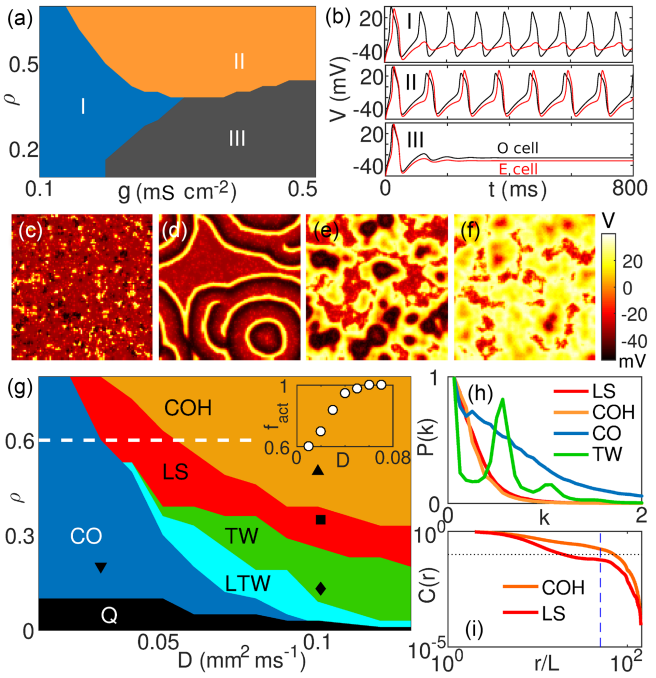

FIG. 2. Heterogeneous media, comprising excitable (E) and oscillatory (O) cells electrotonically coupled to neighbors, display diverse spatiotemporal patterns, with coherent activity emerging only under strong coupling and for relatively higher proportion of oscillatory cells. (a),(b) The collective dynamical regimes observed in the mean-field limit for different values of coupling, D, and relative fraction of O cells, ρ, correspond to: (I) O active, E inactive, (II) both O and E active, and (III) both O and E inactive [O and E are indicated by red and blue curves, respectively, in the time-series shown in (b)]. (c)–(f) Different spatiotemporal activity patterns observed in V for a two-dimensional square lattice ($L = 50$) with ρ fraction of O and $(1-\rho)$ fraction of E cells, neighbors being coupled with strength D: (c) clustered oscillation (CO), (d) traveling waves (TW), (e) localized synchronization (LS), and (f) coherence (COH) (Video S1). (g) Oscillatory activity is suppressed upon decreasing ρ, yielding quiescent state Q. Localized traveling waves (LTW) regime may also be observed, in which the fraction of active cells $f_{\text{act}} < 0.9$ (Video S2). The inset shows the variation of f_{act} with D along the broken line in the main figure to indicate the distinction between CO and LS regimes. The parameter values for the patterns in (c)–(f) are indicated using the markers $\triangledown$, $\diamond$, $\square$, and $\triangle$, respectively. The corresponding states can be distinguished by their (h) power spectrum $P(k)$ and (i) correlation function $C(r)$ [horizontal dotted line: $C(r) = 0.1$; vertical broken line: $r = L/2$, L being the linear extent of the domain].

A complete description of the electromechanical model that couples Eqs. (1)–(3), is in [30].

We consider a square lattice of $L \times L$ cells ($L = 100$ for the simulations shown here, although we have verified that qualitatively similar results can be seen with other system sizes). Of these, a fraction ρ are oscillatory (O) cells capable of spontaneous periodic activation, the remaining cells being excitable (E). The former have I^O_{bas} that are randomly sampled from an uniform distribution bounded between [90, 150], while the latter are characterized by $I^E_{\text{bas}} = 70$. Each cell is coupled diffusively to its four neighboring cells for the simulations reported here. The diffusive coupling strength D is in general a function of space, but is taken to be a constant here except Figs. 3(d) and 3(e), where D has a spatial gradient. The PDEs (1) and (2) are solved using a pseudospectral method [30,35] for the spatial part (spatial resolution $\delta x = 2$ mm) with periodic boundary conditions (PBC), while the temporal evolution of all equations use the Euler method with temporal resolution $\delta t = 0.1$ ms [49]. The domain size does not change over the course of a simulation because of the PBC. For each choice of ρ and D, results have been averaged over 10 realizations.

We begin by exploring the conditions under which the model exhibits collective dynamics characterized by various spatiotemporal activation patterns, in the absence of any mechanical interactions between the cells. To get a broad understanding of the principal regimes that are possible, we use a mean-field description of the medium in which each cell has exactly the same fraction ρ and $1-\rho$ of O and E cells, respectively, among its k neighbors ($k = 4$ for the lattices we have shown results for) [50]. As seen in Fig. 2(a), in this mean-field setting, the system can be in any one of three regimes depending on the density of O cells ρ and the E-O cellular coupling strength g, viz., I: only the O cells show appreciable activity (for low g), II: O and E cells oscillate in phase (for high ρ and g), and III: both cells inactive (for low ρ but high g). These regimes can be intuitively understood as follows: in regime I, the coupling is too weak for the O cells (that exhibit spontaneous activity) to drive the E cells above their threshold, which can be rectified by making the coupling stronger (regime II). However, if the density of O cells is relatively low (regime III), increased coupling leads to a source-sink imbalance such that the gap-junctional current from O cells is shared between too many inactive cells and is insufficient to drive any of the cells over the threshold, resulting in both cell types becoming quiescent.

Collective dynamics analogous to these three regimes can be observed even upon introducing spatial heterogeneity by randomly choosing the fraction of oscillatory neighbors of a cell from a distribution having a mean value ρ. Thus, the clustered oscillations (CO) state obtained in the limit of weak coupling [Fig. 2(c)], in which the O cells are active but are unable to drive all the E cells because of the low value of D, is analogous to Regime I in Fig. 2(a). Note though that for low D, instead of only O cells being active, the variability introduced by heterogeneity results in several small clusters of activity appearing that locally have a high density of O cells. Increasing the coupling strength results in differential outcomes depending on ρ. For a low density of O cells, this leads to cells becoming quiescent (Q) because of source-sink mismatch, analogous to the situation for regime III in the mean-field limit. As ρ is increased, the

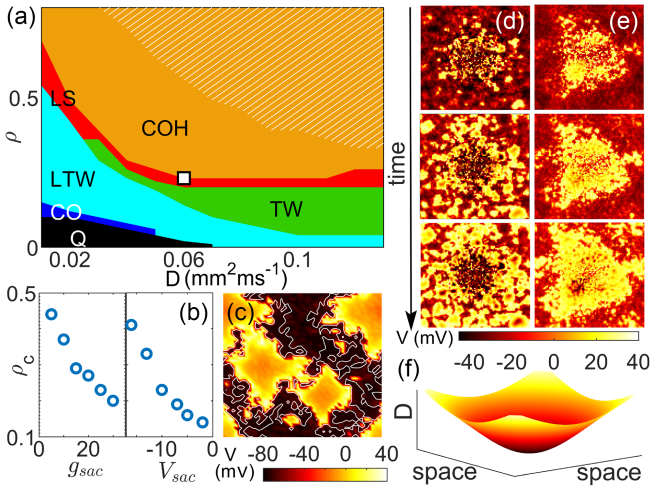

FIG. 3. Mechanical interactions promote synchronization of activity even for extremely weak electrical coupling between cells. (a) In presence of I_{sac} ($g_{sac} = 25, V_{sac} = -10$), COH is observed over a much broader range of parameters ρ and D [for comparison, the hatched region shows its extent in the absence of I_{sac}, see Fig. 2(g)]. The other globally oscillating states ($f_{act} > 0.9$), LS and TW, have extended into the regions that was occupied by the quiescent regime Q and the partially oscillatory CO domain when $g_{sac} = 0$ [see Fig. 2(g)]. The critical value ρ_c of oscillator density at which COH emerges for $D = 0.06$ mm^2 ms^{-1} is indicated (open square). (b) Variation of ρ_c as a function of the conductance g_{sac} [$V_{sac} = -10$] and reversal potential V_{sac} [$g_{sac} = 25$]. (c) Activation pattern in an array of heterogeneous cells ($\rho = 0.37$, $D = 0.1$ mm^2 ms^{-1}) whose ionic currents are described by the more detailed MNT model, in the presence of mechanical interaction. The contour lines indicate the regions ahead of the excitation front where $|I_{sac}| > 0.7$ μF/cm^2. (d),(e) Snapshots indicating the spatiotemporal evolution of V (time increasing from top to bottom) for $g_{sac} = 0$ (d) and 25 (e), respectively. The spatially changing strength of electrical gap-junction couplings is modeled by D varying along a gradient between [0,0.07], increasing radially from the center (f). Comparing (e) with (d), we note that the activity becomes more coherent (particularly in the central region) in the presence of mechanical interactions (Video S3).

relatively strong coupling between cells implies that local clusters having a higher density of O cells act as organizing centers for activity spreading in the form of traveling waves [TW, Fig. 2(d)]. As ρ is increased further, we observe successively larger regions of the domain getting synchronized in their activity in the locally synchronized (LS) regime [Fig. 2(e)], eventually leading to coherence [COH, Fig. 2(f)], such that the periodic activity of cells across the entire domain is occurring in phase, analogous to regime II in the mean-field limit.

The various types of collective dynamics discussed above arise under different conditions of cellular heterogeneity [quantifiable as $\sim\rho(1-\rho)$] and coupling, as seen from the position of the corresponding domains in $\rho - D$ parameter space shown in Fig. 2(g). The inset shows the variation with D in the order parameter f_{act}, i.e., the fraction of cells undergoing persistent oscillations, for maximal heterogeneity in the cellular composition of the domain ($\rho = 0.5$). A transition from CO to LS can be observed when f_{act} exceeds 90% around $D \sim 0.03$. As already mentioned, if the relative density of O cells are decreased, then depending on the coupling strength between cells, we will either see a transition to Q (when $f_{act} < 0.1$) or TW. The latter pattern is of particular relevance for systems such as the sino-atrial node or uterine tissue where they have been observed [27,51] and associated with aberrant functioning [28,52]. The TW regime can be identified by the presence of a characteristic wavelength in the resulting patterns, resulting in a prominent secondary peak [Fig. 2(h)] in the power spectrum $P(k)$ [$= \tilde{V}_k \tilde{V}_k^*$, where $\tilde{V}_k, \tilde{V}_k^*$ are the amplitudes of the kth Fourier mode of $V(r)$ and its complex conjugate]. If we decrease the density of O cells, the waves are eventually confined within spatially disjoint patches ($0.1 < f_{act} < 0.9$), which we refer to as localized traveling waves (LTW) (Video S2).

As reported above, in the strong coupling regime, increasing the fraction ρ of O cells results in the clusters exhibiting spontaneous activity becoming larger in size. This increasing synchronization through the LS and COH regimes is reflected in the reducing width of the mode amplitude spectrum $P(k)$ compared to that for CO [Fig. 2(h)]. The clustering over larger length scales (corresponding to small k) is also shown explicitly by the spatial correlation function $C(r) = \langle V(0)V(r)\rangle - \langle V(0)\rangle^2/(\langle V(0)^2\rangle - \langle V(0)\rangle^2)$ between the activity at a pair of locations separated by a distance r, the averaging being over both the origin and time. The COH regime is distinguished from LS by the correlation length ξ over which $C(r)$ decreases to 10% of its maximum value [Fig. 2(i)]. COH is characterized by $\xi \geq L/2$ (L being the system size), implying that almost all points in the medium are correlated.

On introducing the contribution of mechanical interactions between cells to the electrical activity via I_{sac}, which is modulated by tissue deformation (see above), we observe that synchronization is promoted in the system (the result being invariant with respect to magnitude of the tissue deformation [30,53]). This is evident from the expanded region in the ρ-D parameter space corresponding to COH [Fig. 3(a)] in comparison to Fig. 2(a), as well as the occurrence of LS, TW, and LTW even with extremely weak gap-junctional coupling. The stretch-activated current results in the system being capable of spontaneous periodic activity over almost the entire parameter space, indicated by the significant shrinking of CO and Q. The role of the stretch activated channel parameters, specifically, g_{sac} and V_{sac}, in driving COH can be seen from the decrease in the critical value ρ_c, the minimum relative density of O cells with which coherence can be achieved (for $D = 0.06$), as

the channel conductance and reversal potential are increased, respectively [Fig. 3(b)]. Note that, even when the cellular electrophysiology is described by the more detailed MNT model [Fig. 3(c)], stretch-induced currents enhance synchronization [30].

Mechanical interactions between the cells can also enhance synchronization in tissue where the electrical coupling displays spatial heterogeneity, e.g., a spatial gradient in the gap-junction conductances as reported in the sino-atrial node in the heart [54,55]. Figures 3(d) and 3(e) compare the spatiotemporal evolution of activity in the absence and presence, respectively, of mechanical interactions, in a medium where the electrical coupling D between cells increases radially from the center [as shown in Fig. 3(f)]. At each cycle of periodic excitation, the activity begins in the center. It has the weakest coupling, promoting stimulation by reducing source-sink mismatch between O and E cells. Without the stretch-activated current, however, as this activity spreads outward from the center it gets fragmented because the low density of gap junctions prevents many of the cells from getting excited simultaneously [Fig. 3(d)]. The introduction of I_{sac} provides an alternative mechanism by which cells can excite their neighbors, resulting in a more coherent pattern of spreading activity [Fig. 3(e) and Video S3]. While the simulations shown here are for the case when the oscillating cells are randomly distributed, we have also seen qualitatively similar behavior when the spatial distribution of oscillators is correlated [30].

To conclude, we show that mechanical interactions between cells can work in tandem with electrical intercellular communication via gap junctions to create a robust mechanism for promoting coherent activity in heterogeneous cell assemblies. Indeed, in the limit of weak electrotonic coupling, communication mediated by the physical deformation induced by excitation could be the primary means of coordinating collective behavior of cellular arrays. Our results are consistent with, and may help explain, recent experiments reporting the crucial role that mechanical interactions play in coordinating activity, e.g., in the embryonic heart [56]. Our observation of diverse spatiotemporal patterns can help in understanding emergent collective dynamics in media where ρ and D can vary across space (forming a gradient, as that of gap-junctional density in the sino-atrial node [54,55]) and/or in time under natural or pathological settings (such as, the changes observed in the developing embryonic heart [18,19], the gravid uterus [5,20,21], and progressively fibrotic cardiac tissue [14,22]). The coherence enhancing mechanism described here is based on a very generic model, suggesting that it may be valid for a broad class of systems [6,10,51,57]. Thus our results can provide insights into pathologies associated with breakdown of collective coordination in heterogeneous tissue comprising excitable and oscillatory cells, e.g., the sino-atrial node, the GI tract, and the gravid uterus.

Acknowledgments—S. Z. has been supported by the Center of Excellence in Complex Systems and Data Science, funded by the Department of Atomic Energy, Government of India.

Data availability—The data that support the findings of this article are openly available [53].

[1] D. Bers, Nature (London) **415**, 198 (2002).
[2] P. Langton, S. M. Ward, A. Carl, M. A. Norell, and K. M. Sanders, Proc. Natl. Acad. Sci. U.S.A. **86**, 7280 (1989).
[3] H. Zheng, B. T. Drumm, S. Earley, T. S. Sung, s. D. Koh, and K. M. Sanders, Sci. Signal. (Online) **11**, eaaq0918 (2018).
[4] E. R. Pfeiffer, J. R. Tangney, J. H. Omens, and A. D. McCulloch, J. Biomech. Eng. **136**, 0210071 (2014).
[5] R. C. Young, Reproduction **152**, R51 (2016).
[6] J. D. Huizinga and W. J. Lammers, Am. J. Physiol. Gastr. L. **296**, G1 (2009).
[7] E. Meron, Phys. Rep. **218**, 1 (1992).
[8] S. Sinha and S. Sridhar, *Patterns in Excitable Media: Genesis, Dynamics, and Control* (CRC Press, Boca Raton, FL, 2014).
[9] I. Nitsan, S. Drori, Y. E. Lewis, S. Cohen, and S. Tzlil, Nat. Phys. **12**, 472 (2016).
[10] B. Z. Jia, Y. Qi, J. D. Wong-Campos, S. G. Megason, and A. E. Cohen, Nature (London) **622**, 149 (2023).
[11] K. M. Sanders, L. F. Santana, and S. A. Baker, J. Physiol. (2023).
[12] P. Camelliti, C. R. Green, I. LeGrice, and P. Kohl, Circ. Res. **94**, 828 (2004).
[13] A. V. Panfilov, R. H. Keldermann, and M. P. Nash, Phys. Rev. Lett. **95**, 258104 (2005).
[14] T. P. Nguyen, Z. Qu, and J. N. Weiss, J. Mol. Cell. Cardiol. **70**, 83 (2014).
[15] Y. Okabe, N. Murakoshi, N. Kurebayashi, H. Inoue, Y. Ito, T. Murayama, C. Miyoshi, H. Funato, K. Ishii, D. Xu, and K. Tajiri, Proc. Natl. Acad. Sci. U.S.A. **121**, e2218204121 (2024).
[16] V. Jacquemet, Phys. Rev. E **74**, 011908 (2006).
[17] R. Singh, J. Xu, N. G. Garnier, A. Pumir, and S. Sinha, Phys. Rev. Lett. **108**, 068102 (2012).
[18] M. Watanabe, A. M. Rollins, L. Polo-Parada, P. Ma, S. Gu, and M. W. Jenkins, J. Cardiovasc. Dev. Dis. **3**, 10 (2016).
[19] S. R. Coppen, R. A. Kaba, D. Halliday, E. Dupont, J. N. Skepper, S. Elneil, and N. J. Severs, Mol. Cell. Biochem. **242**, 121 (2003).
[20] J. A. Lenhart, P. L. Ryan, K. M. Ohleth, and C. A. Bagnell, Biol. Reprod. **61**, 1452 (1999).
[21] B. Risek and N. B. Gilula, Development (Cambridge, U.K.) **113**, 165 (1991).
[22] N. J. Severs, S. R. Coppen, E. Dupont, H.-I. Yeh, Y.-S. Ko, and T. Matsushita, Cardiovasc. Res. **62**, 368 (2004).
[23] L. D. Weise and A. V. Panfilov, Phys. Rev. Lett. **108**, 228104 (2012).
[24] G. Bub, A. Shrier, and L. Glass, Phys. Rev. Lett. **88**, 058101 (2002).
[25] G. Bub, A. Shrier, and L. Glass, Phys. Rev. Lett. **94**, 028105 (2005).

[26] A. Kryukov, V. Petrov, L. Averyanova, G. Osipov, W. Chen, O. Drugova, and C. Chan, Chaos **18**, 037129 (2008).

[27] A. V. Glukhov, L. T. Hage, B. J. Hansen, A. Pedraza-Toscano, P. Vargas-Pinto, R. L. Hamlin, R. Weiss, C. A. Carnes, G. E. Billman, and V. V. Fedorov, Circ. Arrhythmia Elec. **6**, 984 (2013).

[28] S. R. Kharche, E. Vigmond, I. R. Efimov, and H. Dobrzynski, PLoS One **12**, e0183727 (2017).

[29] C. Morris and H. Lecar, Biophys. J. **35**, 193 (1981).

[30] See Supplemental Material at http://link.aps.org/supplemental/10.1103/8gqg-rsrl for details, which includes Refs. [31–38].

[31] R. E. McAllister, D. Noble, and R. W. Tsien, J. Physiol. **251**, 1 (1975).

[32] L. D. Weise and A. V. Panfilov, Phys. Rev. Lett. **119**, 108101 (2017).

[33] S. R. De Groot and P. Mazur, *Non-Equilibrium Thermodynamics* (Dover, New York, NY, 1984).

[34] L. A. Taber, *Nonlinear Theory of Elasticity: Applications in Biomechanics*, revised ed. (World Scientific, Singapore, 2023).

[35] C. Canuto, M. Y. Hussaini, A. Quarteroni, and T. A. Zang, *Spectral Methods in Fluid Dynamics* (Springer, Berlin, 1988).

[36] Y. Wang, R. W. Joyner, M. B. Wagner, J. Cheng, D. Lai, and B. H. Crawford, Am. J. Physiol. Heart Circ. Physiol. **296**, H1227 (2009).

[37] M. Buonocunto, A. Lyon, T. Delhaas, J. Heijman, and J. Lumens, J. Physiol. **602**, 4585 (2024).

[38] M. L. Ward, I. A. Williams, Y. Chu, P. J. Cooper, Y. K. Ju, and D. G. Allen, Prog. Biophys. Molec. Biol. **97**, 232 (2008).

[39] K. Tsumoto, H. Kitajima, T. Yoshinaga, K. Aihara, and H. Kawakami, Neurocomputing **69**, 293 (2006).

[40] G. B. Ermentrout and D. H. Terman, *Mathematical Foundations of Neuroscience* (Springer, New York, NY, 2010).

[41] N. H. Kuijpers, H. M. ten Eikelder, P. H. Bovendeerd, S. Verheule, T. Arts, and P. A. Hilbers, Am. J. Physiol. Heart C. **292**, H2832 (2007).

[42] We note that other mechanosensory mechanisms not involving a stretch-activated current have also been proposed to coordinate synchronized activity in cardiac cells, e.g., see Ref. [9].

[43] A. Simon-Chica, A. Klesen, R. Emig, A. Chan, J. Greiner, and D. Grün, A. Lother, I. Hilgendorf, E. A. Rog-Zielinska, U. Ravens, P. Kohl, F. Schneider-Warme, and R. Peyronnet, J. Physiol. **602**, 4437 (2024).

[44] A. Reed, P. Kohl, and R. Peyronnet, Glob. Cardiol. Sci. Pract. **2014**, 19 (2014).

[45] J. Yuval and S. A. Safran, Phys. Rev. E **87**, 042703 (2013).

[46] In general, biological tissue are anisotropic [see C. Cherubini, S. Filippi, A. Gizzi, and R. Ruiz-Baier, J. Theor. Biol. **430**, 221 (2017)] but the qualitative features of the patterns reported here are not crucially dependent on this simplifying assumption of isotropy.

[47] The numerical values for the Lamé parameters used in the simulations reported here are $\lambda = \mu = 0.4\ \mathrm{kg\,mm^{-1}\,ms^{-2}}$.

[48] M. P. Nash and A. V. Panfilov, Prog. Biophys. Molec. Biol. **85**, 501 (2004).

[49] For these values of δx and δt, we obtain a conduction speed of 30 $\mathrm{cm\,s^{-1}}$ for $D = 0.2\ \mathrm{mm^2\,ms^{-1}}$.

[50] We note that such a setting will give results identical to the spatially heterogeneous situation implicit in Eq. (1) in the limit of extremely strong gap-junctional coupling (represented by $D \to \infty$) such that every pair of cells can be considered to be coupled. The system can then be effectively reduced to a pair of O and E elements mutually coupled with strength g, whose membrane potentials, V^O and V^E, respectively, evolve as $C_m dV^O/dt = -I_{\mathrm{ion}} + I^O_{\mathrm{bas}} + kg(1-\rho)(V^E - V^O)$ and $C_m dV^E/dt = -I_{\mathrm{ion}} + I^E_{\mathrm{bas}} + kg\rho(V^O - V^E)$.

[51] W. J. Lammers, H. Mirghani, B. Stephen, S. Dhanasekaran, A. Wahab, M. A. Al Sultan, and F. Abazer, Am. J. Physiol., Regul. Integr. Comp. Physiol. **294**, R919 (2008).

[52] J. Xu, S. N. Menon, R. Singh, N. B. Garnier, S. Sinha, and A. Pumir, PLoS One **10**, e0118443 (2015).

[53] We have made the simulation code available in https://github.com/solingzimik/Electromechanics.

[54] E. E. Verheijck, M. J. van Kempen, M. Veereschild, J. Lurvink, H. J. Jongsma, and L. N. Bouman, Cardiovasc. Res. **52**, 40 (2001).

[55] H. Honjo, M. R. Boyett, S. R. Coppen, Y. Takagishi, T. Opthof, N. J. Severs, and I. Kodama, Cardiovasc. Res. **53**, 89 (2002).

[56] K. K. Chiou, J. W. Rocks, C. Y. Chen, S. Cho, K. E. Merkus, A. Rajaratnam, P. Robison, M. Tewari, K. Vogel, S. F. Majkut *et al.*, Proc. Natl. Acad. Sci. U.S.A. **113**, 8939 (2016).

[57] R. Manchanda, S. Appukuttan, and M. Padmakumar, J. Exp. Neurosci. **13**, 1 (2019).